Journal Pre-proof

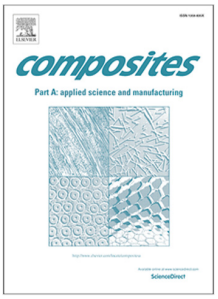

Predicting filling efficiency of composite resin injection repair

Ahmed Asiliskender, Joaquim Peiró, Koon-Yang Lee,
Apostolos Parlamas, Brian Falzon, Zafer Kazancı

PII: S1359-835X(23)00284-1
DOI: https://doi.org/10.1016/j.compositesa.2023.107708
Reference: JCOMA 107708

To appear in: *Composites Part A*

Received date : 26 May 2023
Revised date : 19 July 2023
Accepted date : 24 July 2023

Please cite this article as: A. Asiliskender, J. Peiró, K.-Y. Lee et al., Predicting filling efficiency of composite resin injection repair. *Composites Part A* (2023), doi: https://doi.org/10.1016/j.compositesa.2023.107708.

REVISED Manuscript (revised text MARKED)

Predicting Filling Efficiency of Composite Resin Injection Repair

Ahmed Asiliskender[1*], Joaquim Peiró[1], Koon-Yang Lee[1**], Apostolos Parlamas[2], Brian Falzon[2], Zafer Kazancı[2]

[1] *Department of Aeronautics, Imperial College London, South Kensington Campus London SW7 2AZ, United Kingdom*

[2] *School of Mechanical and Aerospace Engineering, Queen's University Belfast Ashby Building, Belfast BT9 5AH, United Kingdom*

Abstract

We propose to develop a two-dimensional reduced-order reconstruction, simulation and injection strategy to model resin injection repair which is scalable and practical for use with available equipment. The proposed method involves reconstructing a damaged composite laminate using ultrasonic C-scans to determine the damage zone geometry and porosity. The damage zone permeability is calculated via semi-empirical constitutive equations, and used as input data for the CFD simulation of a resin injection process through the composite. The ultimate aim is to guide repair operators by identifying suitable injection configurations in order to improve cavity filling and thus repair efficiency. After establishing the methodology basis, we verify simulations through comparison to a proposed and analytically solved problem. Validation results show a 70+% simulation accuracy. Finally, we create a case study where cavity filling is improved by applying knowledge of the damage zone. This method's ability to predict filling efficacy offers a viable, quantitative and more consistent alternative to existing intuition-based practices for resin injection repair.

Keywords: Laminate Repair, B. Permeability, C. Computational Modelling, C. Process Modelling

*Corresponding author
**Institute for Molecular Science and Engineering
Email addresses: ahmed.asiliskender14@imperial.ac.uk (Ahmed Asiliskender[1]), j.peiro@imperial.ac.uk (Joaquim Peiró[1]), koonyang.lee@imperial.ac.uk (Koon-Yang Lee[1]), aparlamas01@qub.ac.uk (Apostolos Parlamas[2]), brian.falzon@rmit.edu.au (Brian Falzon[2]), z.kazanci@qub.ac.uk (Zafer Kazancı[2])

1. Introduction

The use of composite materials is growing and, in particular, larger and more complex resin-infused composite structures are becoming ubiquitous in a variety of industries, such as aerospace, automotive, and wind energy to name but a few. The constituent material and architecture of these composites often leads to highly complex damage mechanisms after impact [1] that make their repair challenging and costly. There is a range of repair methods that are efficient and reliable in restoring the mechanical properties of composite structures such as fastening methods and bond scarf and patching repairs [2]. These methods are highly invasive requiring either the drilling of holes for fastening additional material which produces an undesirable stress concentration around the holes [3], or the removal of material and surface preparation for adhesive bonding. Bonded repair methods, scarf bond in particular, are arguably the most effective and reliable in restoring mechanical strength [4], but can be costly in time, material, equipment and require skilled labour [5, 6]. Resin injection repair (RIR) is an alternative, less invasive, repair method that involves drilling venting and porting holes to inject a curing resin in the damaged zone [2, 7, 8]. A schematic of a representative RIR set up is shown in Figure 1.

Compared to traditional composite repair methods, RIR can be more cost effective and faster to apply on site with or without vacuum support [2, 9]. RIR is particularly suited for repair of damaged components that will not be subject to tensile loads [8, 9] and can achieve high repair effectiveness in restoring compression-load strength [10, 11, 12]. For example, compression after impact (CAI) strength recoveries of 71-114% have been reported by Moghe *et al.* [11] using epoxy resin on impacted CF-Epoxy composites, and of 76-103% by Thunga *et al.* [12] using BECy (Bisphenol E Cyanate ester) resins to repair damaged bismaleimide (BMI)-CF composites.

Current RIR practices are based on basic guidelines, intuition, and/or trial-and-error experience [13]. To improve them we need to address some of their limitations. The first step in any repair method is to detect the presence of damage and its extent. This can be achieved through a variety of methods, including simple visual or auditory inspection, but of interest to RIR is the use of

non-destructive testing (NDT) techniques, such as ultrasound and thermography, that identify the geometry and severity of the damage [14]. An assessment of the extent and severity of the damage and of the mechanical properties required to repair it determines if RIR is the right repair method [9, 11, 15].

Once RIR is adopted, holes to inject the resin into the cavity and vent it must be drilled into the composite in a manner that causes minimal structural damage [16]. A RIR strategy will define a set of parameters, namely the number of injection and vent holes, and their locations, depth and sizes, as well as the injection pressure. These parameters are often selected using basic rules-of-thumb rather than a rigorous strategy [9, 17, 18]. This may lead to noticeable differences in the effectiveness of RIR [12, 19]. This highlights the importance of parameter selection in repair configurations and their impact on the effectiveness of the RIR procedure. Furthermore, there are no other models for investigating composite RIR; the closest model are composites manufacturing models that use constant porosity such as for RTM [20], and small-scale 3D or 2D models of self-healing composites [21]. To address these issues, we propose the use of a digital reconstruction to simulate the RIR process and to assess its efficacy, with the ultimate aim of allowing end users to achieve optimal repair efficiencies in practical applications. In this paper, we first provide an overview of the approach and describe the main assumptions underpinning the proposed reduced-order model of RIR. The governing equations and their associated physical parameters, properties and conditions of the flow simulation are then described in more detail. A representative benchmark with an analytical solution, utilised for verifying the numerical simulation, is proposed as a contribution of this paper. The process for reconstructing the geometry of the damage zone and its permeability is then documented before applying the method to two given repair cases of impact-damaged panel specimens to undertake validation testing. We also undertake a case study where we make use of the proposed methodology to improve the predicted filling efficiency. Finally, the main outcomes of the investigation are presented and the suitability of the methodology for practical applications is discussed.

2. Proposed Reduced-Order Methodology

Finding an optimal or near-optimal repair configuration in practice is difficult for repair operators because the geometry and characteristics of damaged zones are both intricate and intrinsically different from case to case. This is the main reason why current RIR procedures are based on basic guidelines, intuition or operator experience obtained by trial-and-error. These guidelines involve, but are not limited to, placing one inlet centred on the damage and multiple outlets placed evenly spaced around the periphery of the damage zone. The availability of computational techniques for simulating of a "virtual injection" process offers the possibility of using them to guide the operator in the search for porting and venting configurations leading to increased cavity filling efficacy or, by combining simulations with optimal control, to automatically find optimal configurations.

Since high-fidelity three-dimensional (3D) simulations of the virtual injection process are impractical because their high cost and their reliance on high-resolution scanning equipment, such as CT scanners, we advocate the use of a more cost effective reduced-order model. The model assimilates the damaged cavity to a two-dimensional (2D) porous medium characterised by a depth-averaged porosity field that can be reconstructed using simpler, and more accessible, scanning methods such as ultrasound. Furthermore, reducing the dimensions of the problem to two significantly reduces the computational cost.

On that account, we propose a reconstruction-simulation-injection strategy to RIR. More precisely, we propose a methodology that first creates a 2D reconstruction of a damaged composite through ultrasonic testing. The reconstructed geometry is assumed to have a porous damage zone, with porosity determined by thickness changes due to damage. The porosity is linked to flow properties by means of a constitutive equation, allowing for computational simulations of resin flow through this damage area. The aim of this strategy is to provide repair operators with a cost-effective way to carry out RIR by analysing alternative configurations, assessing the suitability of the adopted porting and venting locations, and calculating estimates of their filling efficiency. The availability of such estimates, if accurate, could ultimately allow non-specialised operators to find optimal or

near-optimal repair configurations [9, 11, 18].

The proposed modelling assumes that the thickness of the composite panel is small compared with the other dimensions and that the damage zone to be injected with resin behaves like a porous material. The key steps of the proposed approach are:

1. The injection process is modelled as a two-dimensional (2D) flow through porous material governed by Darcy's equation.
2. The permeability of the material is calculated from the porosity through a semi-empirical relation.
3. C-scan measurements are used to determine the geometry of the damaged area, and to calculate the porosity from the thickness distribution of the composite panel.
4. The resin flow is simulated via the numerical solution of Darcy's equation of two-phase flow of resin and air.
5. The flow simulation predicts the fill ratio of the damaged area given the injection flow rate and the position of the porting and venting holes.

The methodology proposed is a proof-of-concept for predicting the effectiveness of injection configurations in a given repair process. It is verified against an analytical solution of the axisymmetric Darcy's equation, and is also validated using two experimental impact damage and subsequent repair scenarios.

3. Modelling of the RIR process as a 2D flow through a porous medium

This section presents the governing equations of the model as well as the choices for its parameters. We assimilate the flow of resin within a damaged composite panel to that of the flow of a fluid through an isotropic porous media. Given that the thickness of the panel is much smaller than the other dimensions, we adopt a two-dimensional model of the flow in terms of the thickness-averaged values of the flow variables and characteristic parameters. Inertial effects are neglected as the flow is

expected to be slow and dominated by viscosity (Re < 1). We assume the resin to behave as a Newtonian fluid thus neglecting viscoelastic effects, which is reasonable if the duration of the resin flow is shorter than the resin gel-time. Capillarity is also ignored as it is accounted for as part of porosity. Furthermore, gravity is ignored as the cavity network is thin and so gravitational effects are negligible especially in comparison to viscous effects.

3.1. Governing equation: 2D Darcy's Law

The flow within a porous material where inertial, gravity and capillary effects are negligible is governed by the following form of Darcy's law [22]

$$\mathbf{q} = -\frac{\mathbf{k}}{\mu} \cdot \boldsymbol{\nabla} P \quad \mathbf{q} = \phi \mathbf{u} \tag{1}$$

where $\mathbf{q}$ is the fluid flux, ϕ is the porosity, $\mathbf{u}$ is the resin velocity, $\mathbf{k}$ is the permeability, P is the pressure and μ is the fluid viscosity. In the case of the assumptions taken in this paper, the permeability matrix is assumed to be isotropic and a function of the porosity, ϕ, namely

$$\mathbf{k} = k(\phi)\mathbf{I} \tag{2}$$

where $\mathbf{I}$ is the identity matrix, and $k(\phi)$ is the permeability modulus. The porosity values are obtained from measurements of the thickness field, for which the method is described later in Section 5. The permeability values are obtained by using a permeability-porosity relation, discussed in Section 3.2 that follows.

3.2. Constitutive Relations $k(\phi)$

To proceed, we need to establish a constitutive relationship between the permeability of the material with its apparent porosity. There are a number of semi-empirical equations that can be adapted to characterize the damage zone as a porous material. Here we will focus on three approaches that have been previously proposed as typically representative of composites: the Kozeny-Carman (KC) equation [23], the formulation of Bruschke and Advani [24] and Gebart's formulas [25].

The Kozeny-Carman permability-porosity relation, widely used in groundwater flow literature [23], is given by

$$k(\phi) = \beta \frac{\phi^3}{(1-\phi)^2} \tag{3}$$

where β is a parameter that depends on the geometry of the porous material. This parameter can be obtained through knowledge of the constituent morphology, or through experiments.

The constitutive equation of Bruschke and Advani (BA) [24] was derived specifically for resin transfer moulding simulations. It is based on lubrication theory and describes the permeability of flow across an array of aligned circular cylindrical with parameters that depend on the arrangement of the fibres (i.e. fibre packing). The equation is

$$k(\phi) = \frac{R^2}{c_1} \frac{(1-l^2)^2}{l^a} \left(3l^b \frac{\tan^{-1}\sqrt{\frac{1+l}{1-l}}}{\sqrt{1-l^2}} + \frac{l^2+2}{2} \right)^{-1}; \quad l^2 = c_2(1-\phi) \tag{4}$$

and relates k to the characteristic fibre radius R and parameters a, b, c_1 and c_2 which depend on packing. The pertinent values are shown in [24].

Gebart's approach [25] derives permeability of parallel flow, $k_{\parallel}$, along cylindrical fibres by assuming that the majority of the flow resistance comes from the narrow gaps between the fibres; the equation is nearly identical to Equation (3), but $\beta = 8R^2/c$, which makes it a function of R and a dimensionless shape factor c that depends both on the fibre packing and porosity. The perpendicular flow permeability, $k_{\perp}$, is derived by using a "representative cell" method; the equation relates $k_{\perp}$ to R and c_1. The perpendicular permeability is:

$$k_{\perp} = c_1 R^2 \left(\sqrt{\frac{(1-\phi_{\min})}{(1-\phi)}} - 1 \right)^{\frac{5}{2}} \tag{5}$$

The parameter values used by Gebart for flow in both directions are detailed in [25].

It is important to note that all constitutive equations are also a function of the geometry scale as well as the geometry structure, either directly as with the β term in the KC equation, or indirectly, through geometry assumptions that affect the final equation form as with the other relations mentioned here.

3.3. Comparing Permeability-Porosity Constitutive Relations

Since the porosity-permeability constitutive relation is a principal component to the proposed reduced-order methodology, the simulations of the injection process will depend on the selection of constitutive equation. As we do not have direct data on the permeability, k, of the damaged zone to validate these constitutive equations against our measurements of porosity, in this section we select the constitutive equation to use based on its structure.

As the Bruschke-Advani and perpendicular Gebart equations have a non-zero minimum porosity, $\phi_{\min}$, value ($k_{\phi_{\min}} \to \infty$), these curves do not cover the whole range of $[0, 1)$ porosities. To enforce this, we use the transformation

$$\phi^* = \frac{\phi - \phi_{\min}}{1 - \phi_{\min}} \tag{6}$$

where ϕ^* is a 'modified' porosity that extends to the whole range, i.e. $\phi^* \in [0, 1)$. The modified curves are shown in Figure 2. After applying these transformations, all of the equations show significant similarities in that they are doubly asymptotic (as $\phi^* \to 0$ and $\phi^* \to 1$) and are monotonic functions with gradients that are lower closer to $\phi^* = 0.5$ than towards $\phi^* = 0$ and $\phi^* = 1$. The functions' parameters can be calibrated to a case by using experimental data; and the equations' structural similarity implies the overall permeability distribution will be very similar, with relatively small variations in magnitude. As the KC equation uses a single parameter β that accounts for the morphology of the problem and uses fewer and more general assumptions, we will use the KC Equation (3) to obtain permeability. Although it is possible that β could be a function of many things such as the impact energy, how it is applied, the thickness, size and composition of the composite material, we are not assessing the variation of β with respect to these variables and so will assume for our purposes that β is a constant value in our validation study in Section 6.6 and this value is to be obtained through calibrating the simulation with an experimental result as will be discussed in Section 6.5.

4. Model Verification

This section proposes and describes a verification benchmark that is representative of the two-dimensional two-phase flow simulations to be carried out to model the RIR process. The analytical solution to the problem is derived in Appendix A and is compared here with the numerical simulation in order to verify the proposed methodology.

All simulations were performed using Simcenter STAR-CCM+ (Version 2020.2, Build 15.04.008). A two-dimensional, two-phase flow model is employed, comprising of a liquid (flowing resin) and an ideal gas (air), simulated using the segregated isothermal solver. The numerical treatment of the gas-liquid interface was made robust by applying an interface momentum dissipation model with an artificial interface viscosity setting of 25. The timestep used is 0.1 ms.

The benchmark proposed here is an axi-symmetric injection of resin into a cylindrical cavity containing air. A schematic of the geometry of the domain and a depiction of the initial conditions are shown in Figure 3. The boundary conditions employed in the simulation, together with the computational domain, are shown in Figure 4. The temperature is assumed to be constant throughout the simulation and set at 300 K, the resin and air viscosities are $\mu_l = 150$ mPa s and $\mu_g = 0.01855$ mPa s, respectively, and their corresponding densities are $\rho_l = 1200$ kg m^{-3} and $\rho_g = 1.18$ kg m^{-3}. The properties of air is selected based on publicly available datasheets. The density of the resin is selected based on public datasheets of various epoxy resins, while the viscosity of the resin is selected from datasheets by assuming a processing temperature between 40-60°C. To complete the notation, r_{in} is the radius of the inlet, $r_f(t)$ is the location of the flow front at time t, r_w is the radial location of the end wall, P_{inj} is the injection pressure, and $P_g(t)$ is the air pressure at time t.

The analytical solution to this (quasi-steady) one-dimensional two-phase flow verification problem starts from the axi-symmetric form of Darcy's law

$$\phi u_p = -\frac{k}{\mu}\frac{dp}{dr} \tag{7}$$

where u_p is the velocity and r is the radial coordinate. The pressure is continuous at the gas-liquid

interface since we are neglecting capillary forces. For a constant density flow, conservation mass leads to a velocity

$$u_p(r) = \frac{u_{p,in} r_{in}}{r} \tag{8}$$

where $u_{p,in}$ and r_{in} are the inlet values. Furthermore, the isothermal compression of air, as an ideal gas, means that $PV = \text{cons.}$ where V is the volume of air.

Denoting a dimensionless location of the flow front (which is a function of time) by $\zeta(t) = r_f(t)/r_w$, and ignoring gas losses, the pressure varies only throughout the liquid phase (due to Equation (A.1)), which is rearranged into its integral form with Equation (A.2) applied (with $u_{p,in}$ and r_{in} as the inlet values), solved and non-dimensionalised upon applying Equation (A.3)

$$\begin{aligned} \int_{P_{inj}}^{P_g} \mathrm{d}P &= -\frac{\mu_l \phi u_{p,in} r_{in}}{k} \int_{r_{in}}^{r_f} \frac{1}{r} \mathrm{d}r \\ u_{p,in} &= (P_{inj} - P_g) \frac{k}{\phi \mu_l r_{in} \ln(S\zeta(t))} \\ \overline{u}_{p,in}(\zeta(t)) &= \frac{k}{\phi r_{in}^2 (P_{inj} - P_g(0))} \left(P_{inj} - P_g(0) \frac{1-\zeta(0)^2}{1-\zeta(t)^2} \right) \frac{1}{\ln(S\zeta(t))} \end{aligned} \tag{9}$$

where $S = r_w/r_{in}$ and $\overline{u}_{p,in}$ is a non-dimensional inlet velocity defined as

$$\overline{u}_{p,in} = u_{p,in} \frac{\mu_l}{r_{in}(P_{inj} - P_g(0))} \tag{10}$$

Upon applying the provided parameters, initial and boundary conditions, the analysis detailed in Appendix A leads to an equation describing the inlet velocity as

$$\overline{u}_{p,in}(\zeta) = \frac{10^{-3}}{\ln(30\ \zeta(t))} \left(2.254 - 1.496 \frac{1}{1-\zeta(t)^2} \right) \tag{11}$$

and an implicit equation for the flow front trajectory, $\zeta(t)$, given by

$$\begin{aligned} t =& 0.196\ \mathrm{Li}_2(2.97\zeta^2) - 0.392\ \ln(2.97\zeta^2 - 1)\ \ln(30\zeta) \\ & - 2.98 \times 10^4 \zeta^2 (2\ \ln(30\zeta) - 1) - (0.313 - 0.854i) \end{aligned} \tag{12}$$

where Li_2 is the dilogarithm function (see equation (A.11)). Since t in this expression is a complex number, the physical time is given by its real component.

Figure 5 compares the simulated and analytical curves representing the inlet velocity $\overline{u}_{p,in}(\zeta)$ and

the flow front position, $\zeta(t)$. A mesh convergence study is also shown in Figure 5b. The comparison shows excellent agreement of the analytical solution with the mesh-converged simulation.

Note that the flow front radius does not exceed 60% of the outer domain radius (indicating a fill ratio of $< 36\%$) as the air is being compressed and resisting flow front expansion; this demonstrates the importance of using vacuum for RIR. In fact, if we consider this simulation as a resin injection case with only one injection port, this shows that the minimum fill ratio achieved by an injection is related to the vacuum to injection pressure ratio.

5. 2D Reconstruction from C-scans

This section explains how the reconstruction of the boundary of the damaged area and the evaluation of the spatial distribution of porosity, i.e. the porosity map, was accomplished. We describe how porosity is evaluated through C-scans first, followed by the main sources of information. Next, we detail the material and equipment used. Finally, we describe the data processing strategy and then the steps used to convert the raw information into a usable porosity map.

5.1. Porosity Evaluation

This section describes how to obtain the geometry of the damaged zone and its porosity in the context of a real case: a damaged specimen to be scanned. Then a realistically evaluable method is defined for obtaining the geometric information required by the permeability constitutive equations.

Porosity by definition is the ratio of a volume that is a void, or not of a solid substance. For this 2D model, we take the 'representative' porosity at a location on a composite specimen to be as the ratio of the void thickness to the total thickness. Porosity values are different for a specimen prior to, and after, damage has been received. The key point of our method to determine porosity works by detecting damage along a specific depth in the composite in layers, and any the thickness of any layer(s) that detect damage is taken to be voids. The processing details are explained in Section 5.4, but this means that our model does not measure thickness directly but rather estimates it in order

to seek an approximate calculation of 'effective' porosity created through voids that would allow for resin flow.

There are two key assumptions prior to evaluating the porosity. The first is that undamaged composites have 0% porosity prior to damage as structural composites are produced with minimal voids and any existing voids are negligible, at least in comparison to the amount that is introduced due to damage. The second is that there is no significant loss of composite material due to damage; as such this evaluation will not be accurate in cases such as those of heavy impact damage or perforation where significant material is lost around the impact zone or behind the impacted surface.

The assumption of material conservation is essentially that the amount of composite material remains the same along the thickness, T, prior to and after damage

$$(1 - \phi_{pre})T_{pre} = (1 - \phi_{post})T_{post} \tag{13}$$

where the subscripts *pre* and *post* indicate pre-damage and post-damage states, respectively. Rearranging Equation (13) along with applying the initial 0% porosity assumption provides us with the equation that defines the post-damage porosity as:

$$\phi_{post} = 1 - \frac{T_{pre}}{T_{post}} \tag{14}$$

The post-damage thickness is defined as

$$T_{post} = T_{pre} + \sum_{L=1}^{m} T_{void,L} \tag{15}$$

where the void thickness $T_{void,L}$, of each layer L out of m total layers that scans the inside of the composite, is assumed as the depth range of scan layer when detecting damage, and zero when not.

5.2. Data Sourcing

In order to simulate a realistic case, the data of a real composite specimen has to be obtained. The pre-damage thickness field is obtained here by utilising the knowledge of the specifications of the designed composite structure; depending on the design, this field may be a constant value (within a tolerance value) or may vary. Ultrasonic C-scan testing is used on the front (impacted) face of the

specimen and the C-scan data is then put through processing in order to obtain the post-damage thickness field, which is discussed in Section 5.4. Following this, the porosity is obtained as discussed earlier in Section 5.1.

5.3. Material Sourcing

The two composite specimens used as an example case in this study were created using an IM7/HexPly® 8552 fibre / resin composite composed of 32 laminae of $[45/0/\text{-}45/90]_{4s}$ layup each being 0.131 mm thick for a total thickness of 4.19 mm, with planar dimensions of 150 mm by 100 mm. The specific count of plies and sequence of quasi-isotropic layup is suggested by the ASTM D7136 / D7136M-15 impact test standard. A quasi-isotropic layup is used (as opposed to cross-ply) as it provides strength and stiffness regardless of the direction in which the material is loaded; a damaging impact event can occur at various angles on a composite structure.

The damage was applied to both panels according to the ASTM D7136 / D7136M-15 impact test standard with an impact energy of 24 $\pm$1 J; we label these panels 'Panel 1' and 'Panel 2'. The ultrasonic C-scan testing of the panels is conducted using a Triton 1700TT ultrasonic immersion tank connected to a computer equipped with data acquisition software and a Technisonics immersion probe. The probe is 30 mm long with a diameter of 0.375" (9.5 mm) and operates at a 10 MHz scanning frequency.

5.4. Data processing

The raw A-scan data obtained from the ultrasonic immersion tank is initially processed in the native scanning application into a C-scan mainly through using processing parameters such as signal amplitude threshold for identifying surfaces. We use 7 signal gates with their own threshold values to extract surface signals from noise, creating 7 C-scan datasets per scan with one used for the external front (scanned) face and the other 6 used to seek internal damage surfaces within a certain, mutually exclusive, depth range. The selection of the threshold value is important, discussed later in Section 6.4.

The C-scan data is further processed in order to provide a usable porosity field. Information regarding the specimen size, scan parameters (such as the size of the scan pixels in mm etc.) and the processing parameters are required. New datasets are produced by first omitting the background data. After this, the specimen scan images are corrected for in-plane rotation (and orientation). Once this is done, the void thickness is calculated by using the damage signals obtained from the C-scan's 6 internal gate datasets. For each pixel, the void thickness is as described in Section 5.1, for each gate it is the depth range of the signal gate that identifies damage, and zero for any gate that does not.

Once the void thicknesses are obtained, the values must be scaled to represent the correct distance between the ultrasonic probe and the specimen surface. The scaling applied is simply the ratio of the actual undamaged thickness of the specimen (which is known) to the apparent thickness observed from the C-scan. The post-damage thickness is simply the sum of all the void thicknesses and the pre-damage thickness, accounting for any scaling errors/calibration while assuming that the unscanned thicknesses (not assessed by gates) have no damage, i.e. 0% porosity. This is then used to calculate the porosity obtained through Equation (14) provided in Section 5.1.

After obtaining the porosity there could be points or regions with negative porosity values (possibly due to the corrections applied in previous steps or errors in scanning), this is adjusted for by setting them to zero. Finally, if there are still notable artefacts around and outside the damage zone (where there could be significant non-zero porosity values), such disconnected zones that contain fewer than a small number of cells (less than 100-1000 cells) are excluded from the simulation; such a filtering would be applied regardless in an effort to streamline the simulation.

6. Application of the Reduced-Order Methodology

Here the proposed methodology is applied to realistic cases of damaged composite specimens described previously in Section 5.3. The porosity field reconstructions of the two panels are presented. Then, the repair process undertaken for the two panels is described. Following this, we explain how

we assess the simulation results for practical use and for validation purposes, and subsequently we describe how both the scan threshold and the β parameter is selected and calibrated. Next, the prior set-up is used to validate the proposed process against the two panels. Finally, the methodology is used to examine a case study with the aim of applying information deduced from reconstruction and prior results, with the intent to improve the predicted fill efficiency.

6.1. Damage Zone Porosity Field Reconstruction

The post-processing of the C-scan (described in Section 5.4) results in the porosity maps shown in Figure 6. These porosity maps are used with the KC equation to provide the permeability fields, shown in Figures 7a and 7b. Note that the grey region shown near the centre of impact indicates the region is effectively impervious, even if damage exists. The resulting computational domain used in the STAR-CCM+ simulations is shown in green in Figures 7c and 7d, also showing in cream colour the regions that have not been included in the computational domain either as they are too small or suspected to be artefacts. The injection configuration of the real repairs (described in Section 6.2) is also shown in red and blue, indicating injection and vent ports respectively.

6.2. Injection Experiments

In order to demonstrate the proposed process, we undertake RIR on the two panels described in Section 5.3 upon which we will conduct validation tests. The injection configurations are shown in Figures 7c and 7d in the previous section, which also shows the simulation domain geometry. The 1 bar pressure difference used in the injection from using a vacuum pump is achieved in a few seconds and is maintained for 8 minutes. In both cases, there were 6 injection ports and 3 outlets vents that were grouped to either side with one injection port at the impact point in the center of the panel, and all other holes being angularly equidistant (45°) with radial distances not necessarily equal. Use of multiple injection ports and such grouping of holes is selected as preliminary observations of experiments using the central hole as inlet and all other (periphery) holes as outlets – as per 'traditional' guidelines – showed ineffective resin filling, while this configuration showed much greater infil-

tration.

6.3. Assessing the Simulation Accuracy Index

In order to compare the simulation results to the experimental results, we must be able to compare regions where the damage zone has been filled. We define a quantity of interest called the simulation accuracy index, S_{acc}, by assigning a weighted accuracy value to each cell numbered i, in a simulation domain containing n cells, which is then averaged out according to their weights w_i

$$S_{acc} = \sum_{i=1}^{n} w_i(1 - |f_{exp,i} - f_{sim,i}|) \Big/ \sum_{i=1}^{n} w_i \tag{16}$$

where $f_{exp,i}$ and $f_{sim,i}$ are the resin volume fractions of each cell i according to experimental and simulation results, respectively. Meanwhile, w_i is simply the void volume of each cell, $w_i = T_{void,i}\ s_{c,i}$ where $T_{void,i}$ is the void thickness at cell i and $s_{c,i}$ is the surface area of cell i. The quantity of interest for practical use, the fill efficiency F, is defined as

$$F = \sum_{i=1}^{n} w_i f_i \Big/ \sum_{i=1}^{n} w_i \tag{17}$$

which will also be compared case-by-case for validation. A high S_{acc} means the filling pattern as well as fill ratios, F, as obtained from experiments and simulation (F_{exp} and F_{sim}, respectively) are similar as S_{acc} is a stricter criteria for validation than F.

6.4. Selecting Scan Threshold

The scan threshold is primarily used to eliminate noise from the scan, thus to completely remove noise we used threshold values that are a percentage above a noise baseline threshold (or NBT) where noise appears in less than approximately 5% of the undamaged areas of the composite. However, many characteristics of the outputted scan and subsequent simulation results are sensitive to the threshold which is itself a function of the scanning technique. Therefore, we select a threshold value for all scans (as the same technique and equipment is used) where the scan is least sensitive to the threshold. We define 'sensitivity' of a dependent variable y to an independent variable x is taken to be $\frac{1}{y}\frac{\mathrm{d}y}{\mathrm{d}x}$, the proportional rate of change of y against x.

A damaged specimen was used to study these variables in order to select the threshold value which is then used for subsequent scans and simulations. The primary quantity of interest tested to select for is the simulation accuracy index, while the supporting quantity is the experiment derived fill efficiency. Upon simulating the repair scenarios using threshold values between 40-325% above NBT, S_{acc} ranging between 61-71% were recorded, and that the simulation accuracy index is least sensitive to changes in threshold values around 150-225% above NBT; we selected 200% above NBT to be used in the following simulations as it is the sample point with the lowest sensitivity value while having a flat curve. The experimental fill efficiency and its sensitivity curves shows similar behaviour and thus supports our selected threshold value. We did not select 225% above NBT despite the lower sensitivity magnitude for both values as the sensitivity curves show instability starting around 225% above NBT and are thus unreliable.

6.5. Calibrating Beta β and Permeability Field

As we assume β is constant as mentioned in Section 3.3, we select one panel repair case to calibrate β such that the value used in the simulation, provides the highest simulation accuracy index (or first peak) at the (earliest possible) injection end time. This ensures the simulation fill ratio represents the experimental results as faithfully as possible while ensuring the real and calibrated permeability magnitude of the damage zone are approximately equal, providing relatively accurate infiltration timings. We present the variation of simulation end state fill efficiency with β in Figure 9a. The value of β is inversely proportional to how fast the simulated injection progresses with respect to time – with effectively no change in fill distribution history, despite the existence of a non-trival geometry and porosity field. As a result, β calibration was relatively simple, providing a value of $\beta = 9.1 \times 10^{-9}$ m^2. This beta value results in the permeability fields used for the simulations shown in Figures 9b and 9c.

6.6. Process Validation

In order to confirm the accuracy of our proposed method given scenarios must be compared to known experimental results. Here we present the two real injection cases, described in Section 6.2, that are compared to simulations of the scenario using the calibrated β value provided in the previous section ($\beta = 9.1 \times 10^{-9}$ m^2).

Filling efficiency is calculated for only the simulation domain (Figures 7c and 7d). To avoid potential numerical oscillations and to replicate evacuation of air, the pressure difference between the injection ports and outlet vents were smoothly increased over a period of 6 s, from 0 Pa to its final value (1 bar). The simulations are considered completed when the simulated injection times reach the injection duration in the experiments (8 minutes). The simulations show that the Reynolds number of the flow is always below 1, supporting the use of the Darcy's law form shown in Equation (1) for flow modelling.

The results of the simulation are shown in Figure 10. By comparing the fill patterns during simulation as seen in Figures 10a and 10b with the experimental results seen in Figures 10c and 10d, we obtain the S_{acc} curve in Figure 10e, which shows simulation accuracies of 73% and 77% for Panels 1 and 2 respectively. Figure 10f shows the fill efficiency evolution against the experimental fill efficiency. The experimental fill efficiency and the final simulated fill efficiency of Panel 1 is 90% and 80%, respectively, and for Panel 2 this is 93% and 87%. The validation results are promising as a 70+% accuracy is reasonable considering there are currently no other predictive methods for assessing injection repair success or failure. It should be noted however, that in order to improve the positioning of the holes, the absolute or exact filling efficiency values may not be needed, but rather trends in terms of better or worse configurations of holes.

6.7. Simulation Study Case

In the case presented here we study the impact of intentional hole placement by attempting to improve the predicted fill efficiency conducted on the Panel 1 validation case through intentional and informed hole placement. The relevant images for the study are all shown in Figure 11.

Filling efficiency is a function of the number and location of ports and vents, and by the spatial distribution of permeabilities and damage zone geometry as these determine the effectivenesses of flow paths. Because of these factors, unfilled regions can occur if either there is no feasible flow path to take in order for the resin to infiltrate an area, or the resin flow is too slow to infiltrate. The resistance (the inverse of effectiveness) of such flow paths are some function of the path length, the permeability along the path and the pressure gradient along the path and thus determine the speed of infiltration. Due to these dependencies, outlet vents can be less effective if other vents are interposed on or near a flow path used by it, as it reduces the pressure gradient to leading up to the outlet vent. Furthermore, small passages for resin flow significantly reduces flow effectiveness as large velocities (caused by constriction) impacts the remaining pressure available for resin flow. Both of these cases can be observed in Figures 11a, 11c and 11e where despite the apparent proximity of the bottom-left vent, the resin does not reach the vent in the injection time-frame due to pressure loss. Similarly, no resin reaches near the left vent as the bottom-left vent is present near flow paths already in use.

Taking these reasons into account, as well as the damage geometry and the results from the validation simulation, we change the injection configuration by distributing the outlet vents more evenly instead of having either group to one side; and move the holes outward or inward such that the previously unfilled regions is likelier to be filled. The configuration change is indicated in Figure 11g. The holes in the unfilled regions will be injection ports, and the angular distribution of holes is still even. The new simulation results are shown in Figures 11b, 11d and 11f.

Upon examining the filling efficiency evolution plot illustrated in Figure 11h, noticeable differences between the two curves arise which can be explained by studying the images of filling progression Figures 11a to 11f. In the early stages of the injection process (around 20s, Figures 11a and 11b), we already observe significant differences in the fill ratios of 9.9%. This is due to the fact that the new configuration has ports (and vents) placed on regions with higher permeability, and also distributed outlet vents more evenly, allowing for overall higher pressure gradients and thus flow rates,

accelerating the filling rate.

Approaching the middle stages of injection (100s and onwards, Figures 11c and 11d), the difference in fill ratios continue to increase to 18.9%, and while the fill ratio of the previous configuration begins to level off, the newer configuration maintains a high fill rate. This is due to the fact that the wider distribution, and overall increase in distance between the injection ports and outlet vents from reconfiguration cause the fill rate to be maintained for longer.

Due to the previous described differences in the original and new hole placements, towards the end of the injection process (Figures 11e and 11f) there are marked differences in either configuration; the original configuration has a lower fill ratio but the fill rate has not levelled off while the newer configuration has levelled off completely and also has shows a higher fill ratio. Even if the original configuration could still reach a similar fill ratio, its sub-optimal placement of holes would mean that it would happen over a drastically longer time-frame.

Thus, the results show that intelligent placement of holes provides a significant improvement to the filling process and its effectiveness, as the new configuration indicates a filling ratio of about 98%, compared to the original configuration simulation result (used in validation) of 80%. However, this result is only the prediction of the simulation, and validating the efficacy of the process using a given simulation result (rather than vice versa) requires further testing.

7. Key Findings and Conclusions

We have proposed a predictive, simulation-based strategy that aims at improving the reliability and efficacy of the resin injection repair (RIR) process. The outlined strategy incorporates 2D flow simulation with available technologies for reconstruction and injection to devise a practical method for assessing filling efficiencies for a given set of ports and vents. We compared and selected a constitutive equation to use for the model. Then, we validate the model by presenting an encompassing, multi-model problem and analytically solving it. After detailing the steps for reconstruction, the scanning and constitutive parameters are calibrated and the model is then validated with simulation

accuracy indices of 70+%. In our view, this proof-of-concept provides significant improvements in reliability and efficacy and thus leads to a more robust and appealing approach to RIR.

The effectiveness of the methodology has been assessed through the validation cases as well as a case study, from which we have identified a few key findings. Our study of the constitutive equations show these equations are similar in structure and thus the distribution of permeability values are alike; simply selecting one and calibrating parameters to experimental data is accurate enough. In our approach of calibrating β, we also observe that variations in β do not change the filling distribution, only scale the time required for an infiltration, making calibration simple.

The verification simulation reinforces the significance of maintaining a low vacuum to injection pressure ratio as it increases the minimum filling achieved while the validation scenarios simulations demonstrate the importance of effective resin flow paths. Finally, the analysis of the validation simulation results and the following case study show us that for RIR to be more effective and improve cavity filling, the position of ports and vents should be placed based on gathered knowledge. Placing holes in high permeability areas, and distributing them more widely and evenly enable resin flow to be faster but careless placement of a vent may render other vents less effective if interposed on or near a resin flow path. The ability of the method to predict filling efficiencies offers a viable, quantitative and more consistent, alternative to existing intuition-based practices for determining injection and outlet port configurations.

Acknowledgements

This research was supported by a grant from Dstl for a 3 Year Research PhD titled 'Design and Optimisation of Nano-Modified Liquid Resin Injection Strategy for Maximum Composite Repair Efficiency'. The research was monitored by Luke Rumsey and Kevin Denham to whom we are thankful for arranging the fruitful collaboration with QUB, and for their support, encouragement, expert advice and feedback.

References

[1] V. Giurgiutiu, Chapter 5 – Damage and Failure of Aerospace Composites, Academic Press, Oxford, 2016. doi:10.1016/B978-0-12-409605-9.00005-2.

[2] S. Halliwell, Repair of fibre reinforced polymer (FRP) structures, Tech. rep., National Composites Network (2012).
URL https://compositesuk.co.uk/system/files/documents/repairoffrpstructures.pdf

[3] W. L. Lai, H. Saeedipour, K. L. Goh, Experimental assessment of drilling-induced damage in impacted composite laminates for resin-injection repair: Influence of open/blind hole-hole interaction and orientation, Composite Structures 271 (August 2020) (2021) 114153. doi:10.1016/j.compstruct.2021.114153.
URL https://doi.org/10.1016/j.compstruct.2021.114153

[4] K. B. Katnam, L. F. Da Silva, T. M. Young, Bonded repair of composite aircraft structures: A review of scientific challenges and opportunities, Progress in Aerospace Sciences 61 (2013) 26–42. doi:10.1016/j.paerosci.2013.03.003.

[5] Ziegler Aerospace, Cost of Maintaining Composites Can Offset Performance Gains.
URL https://ziegler-aerospace.co.uk/cost-of-maintaining-composites-can-offset-performance-gains/

[6] C. Lester, S. Nutt, Composite Materials: Advantages and Cost Factors, Tech. rep. (2018).
URL http://www.elevatedmaterials.com/wp-content/uploads/2018/04/White-Paper-1-CFRP-Advantages-Cost-Factors.pdf

[7] W. L. Lai, H. Saeedipour, W. L. Wong, K. L. Goh, In situ resin-injection approach for repairing barely visible impact damaged carbon-fiber reinforced epoxy laminates: Optimizing the repair parameters using Taguchi method, Polymer Composites (March) (2023) 3372–3386. doi:10.1002/pc.27327.

[8] J. Li, Micro-nozzle resin injection repair for polymer composites: A review, Ph.D. thesis, Imperial College London.

[9] R. S. Pierce, N. Campus, B. G. Falzon, Injection repair of composites for automotive and aerospace applications, in: 21st International Conference on Composite Materials, Xi'an, 2017.

[10] A. J. Russell, C. P. Bowers, Repairing Delaminations with Low Viscosity Epoxy Resins, in: AGARD Conference Proceedings No. 530, Patras, 1992, pp. 216–225.

[11] R. P. Moghe, R. Prakash, D. Sudevan, H. K. Shambhayya, Characterization of resin-injection repair of impact damage in polymer matrix composite, in: ASME 2015 International Mechanical Engineering Congress and Exposition, 2015, pp. 1–9. doi:10.1115/IMECE2015-50400.

[12] M. Thunga, K. Obusek, R. Meilunas, M. Akinc, M. R. Kessler, A. Bauer, Injection repair of carbon fiber/bismaleimide composite panels with bisphenol E cyanate ester resin, Composites Science and Technology 100 (2014) 174–181. doi:10.1016/j.compscitech.2014.05.024.

[13] FAA, Aviation Maintenance Technician Handbook-Airframe, Volume 1 (FAA-H-8083-31A), 2018.
URL https://www.faa.gov/regulations_policies/handbooks_manuals/aviation/

[14] M. Thunga, A. Bauer, K. Obusek, R. Meilunas, M. Akinc, M. R. Kessler, Injection repair of carbon fiber/bismaleimide composite panels with bisphenol E cyanate ester resin, Composites Science and Technology 100 (2014) 174–181. doi:10.1016/j.compscitech.2014.05.024.

[15] P. G. Slattery, C. T. McCarthy, R. M. O'Higgins, Assessment of residual strength of repaired solid laminate composite materials through mechanical testing, Composite Structures 147 (2016) 122–130. doi:10.1016/j.compstruct.2016.03.036.

[16] W. L. Lai, H. Saeedipour, K. L. Goh, Mechanical properties of low-velocity impact damaged carbon fibre reinforced polymer laminates: Effects of drilling holes for resin-injection repair,

Composite Structures 235 (November 2019) (2020) 111806. doi:10.1016/j.compstruct.2019.111806.

URL https://doi.org/10.1016/j.compstruct.2019.111806

[17] P. G. Slattery, C. T. McCarthy, R. M. O'Higgins, Development of a novel cyanoacrylate injection repair procedure for composites, Composite Structures 153 (2016) 1–11. doi:10.1016/j.compstruct.2016.05.101.

[18] V. S. Balakrishnan, H. Seidlitz, Potential repair techniques for automotive composites: A review, Composites Part B: Engineering 145 (December 2017) (2018) 28–38. doi:10.1016/j.compositesb.2018.03.016.

[19] A. E. Bauer, Injection repair of advanced aircraft composites with a high temperature cyanate ester resin, Ph.D. thesis, Iowa State University (2013).

URL http://lib.dr.iastate.edu/cgi/viewcontent.cgi?article=4048&context=etd

[20] B. Liu, S. Bickerton, S. G. Advani, Modelling and simulation of resin transfer moulding (RTM)—gate control, venting and dry spot prediction, Composites Part A: Applied Science and Manufacturing 27 (2) (1996) 135–141. doi:10.1016/1359-835X(95)00012-Q.

URL https://linkinghub.elsevier.com/retrieve/pii/1359835X9500012Q

[21] J. Hall, I. P. Qamar, T. C. Rendall, R. S. Trask, A computational model for the flow of resin in self-healing composites, Smart Materials and Structures 24 (3). doi:10.1088/0964-1726/24/3/037002.

[22] A. Verruijt, Theory of Groundwater Flow, 2nd Edition, Macmillan, 1982. doi:https://doi.org/10.1007/978-1-349-00175-0.

[23] W. L. McCabe, J. C. Smith, P. Harriot, Unit Operations of Chemical Engineering, 7th Edition, McGraw-Hill, New York, 2005. doi:10.1016/0016-0032(57)90777-9.

[24] M. V. Bruschke, S. G. Advani, Flow of generalized Newtonian fluids across a periodic array of cylinders, Journal of Rheology 37 (3) (1993) 479–498. doi:10.1122/1.550455.

[25] B. R. Gebart, Permeability of Unidirectional Reinforcements for RTM, Journal of Composite Materials 26 (8) (1992) 1100–1133. doi:10.1177/002199839202600802.

Figure(s) (Revised)

Figure Captions

List of Figures

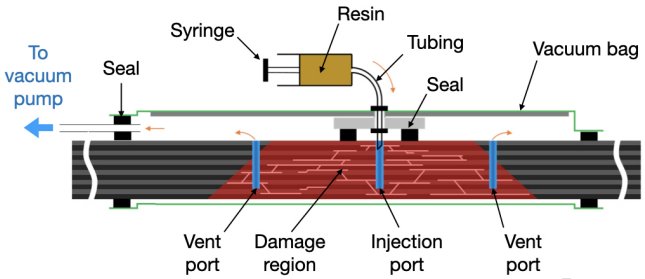

Figure 1: A cross-sectional view of a representative resin injection repair setup.

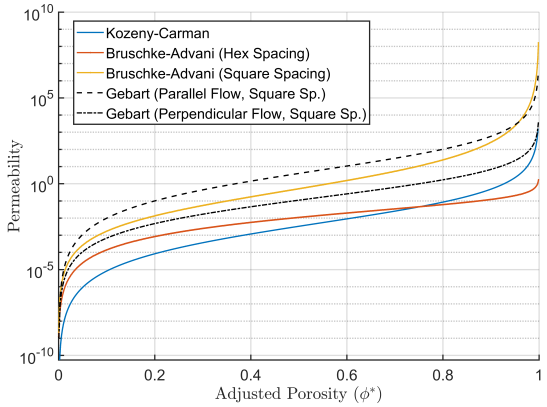

Figure 2: A comparative plot of all discussed porosity-permeability constitutive relations with parameters set to 1.

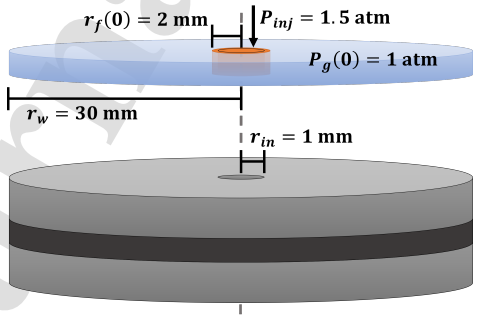

Figure 3: A schematic of the verification simulation domain and its dimensions. The top object shows the initial conditions (air is light blue and resin orange) and the bottom object shows the representative geometry (note that the dark grey shape seals the ends of the annulus from any flow).

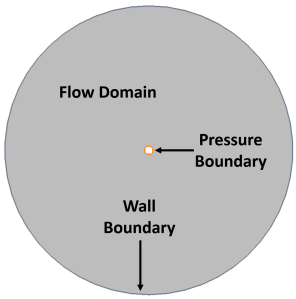

Figure 4: Boundary condition set-up of the domain used for the verification simulation.

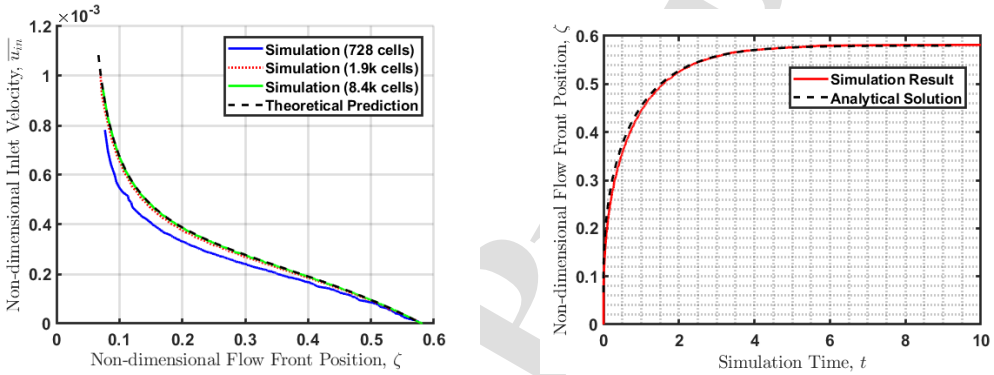

(a) (b)

Figure 5: Verification of the simulation results by comparison to the analytical solution: (a) inlet velocity against flow front position with mesh convergence study; and (b) flow front position against simulation time.

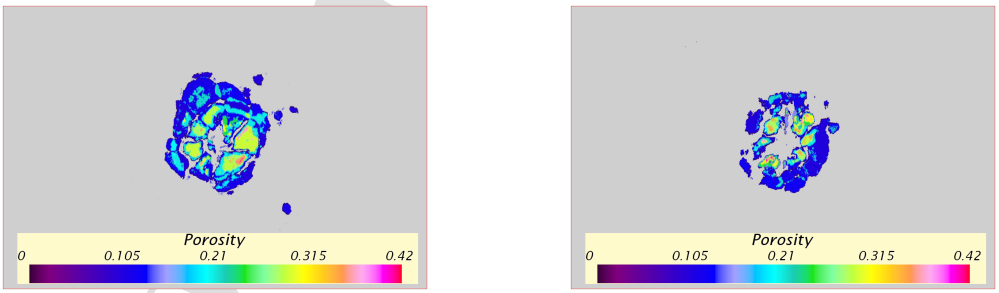

(a) (b)

Figure 6: Ultrasonic C-scan results of the composite specimens: Porosity and damage geometry obtained after post-processing steps of (a) Panel 1 and (b) Panel 2. The grey rectangular area represents the composite panel.

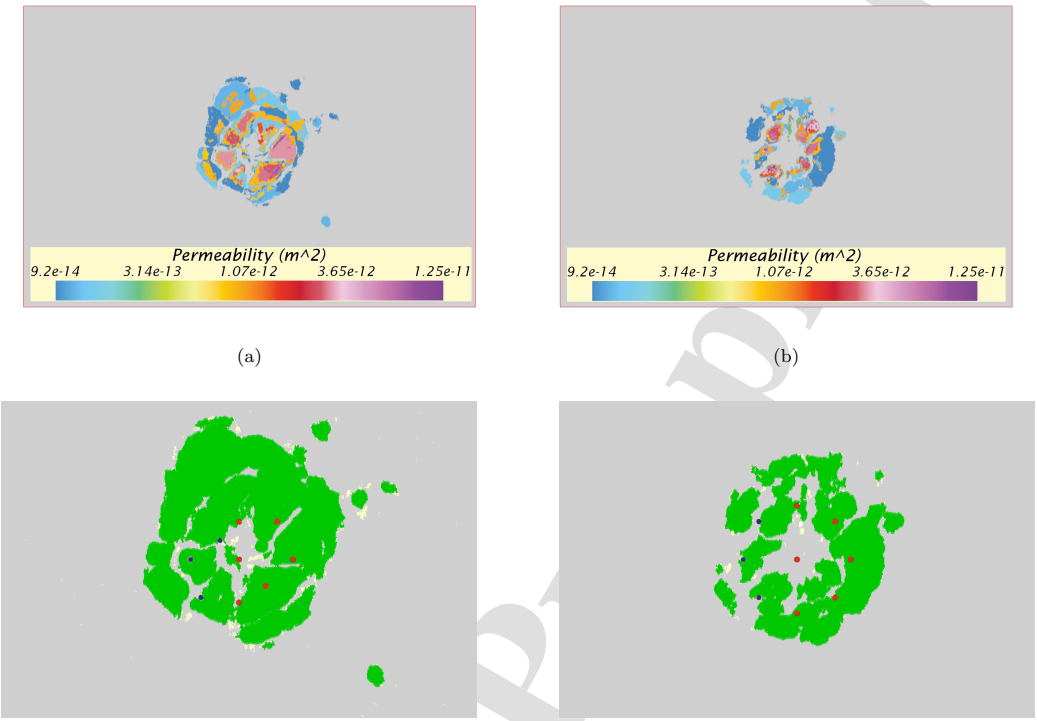

(a) (b)

(c) (d)

Figure 7: Computational domain: Permeability fields of (a) Panel 1, and (b) Panel 2; and simulation domain for (c) Panel 1 and (d) Panel 2. Cream-colored regions are disconnected from the primary damage zone(s) shown in green and are not used in simulations. Red dots indicate injection ports and blue dots indicate outlet vents, this convention is used in all cases.

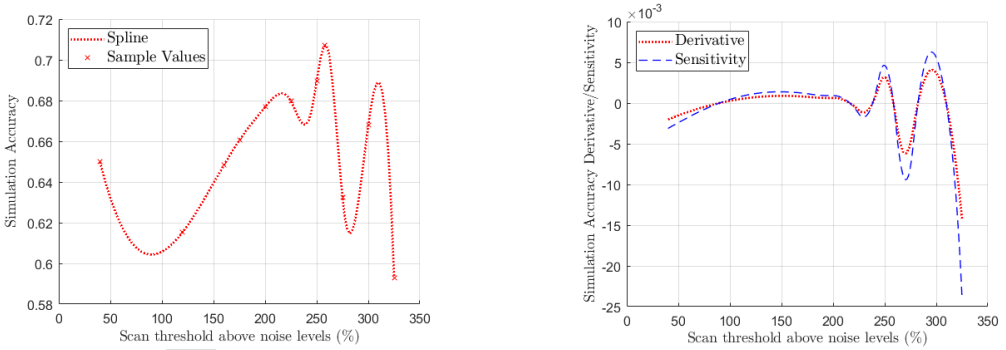

(a) (b)

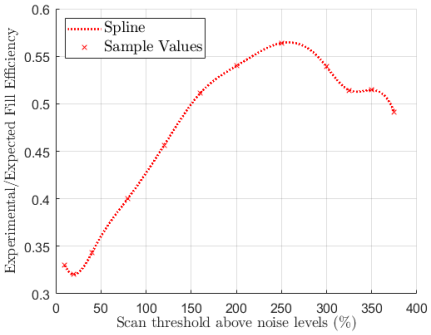

(c)

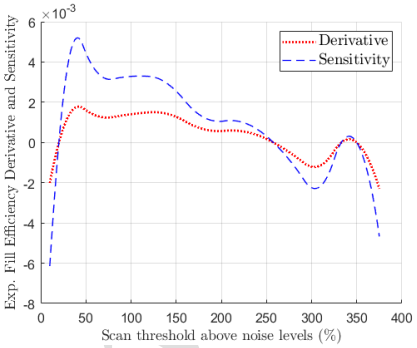

(d)

Figure 8: Threshold value comparisons: (a) simulation accuracy; (b) simulation accuracy derivative and sensitivity; (c) expected fill efficiency (from post-repair scan results); and (d) expected fill efficiency derivative and sensitivity.

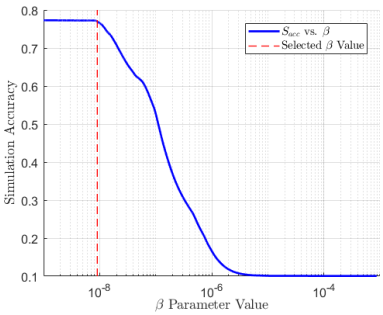

(a)

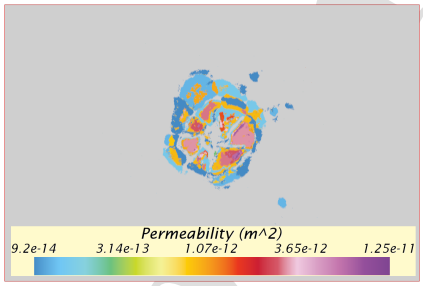

(b)

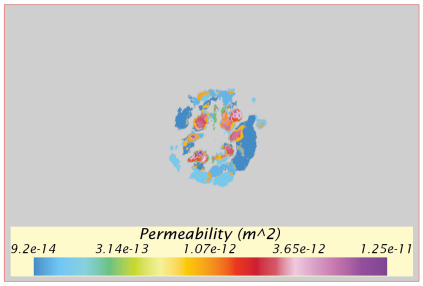

(c)

Figure 9: Calibrating β: (a) β vs. final fill eff. values alongside selected β; and the resulting permeability maps of (b) Panel 1 and (c) Panel 2.

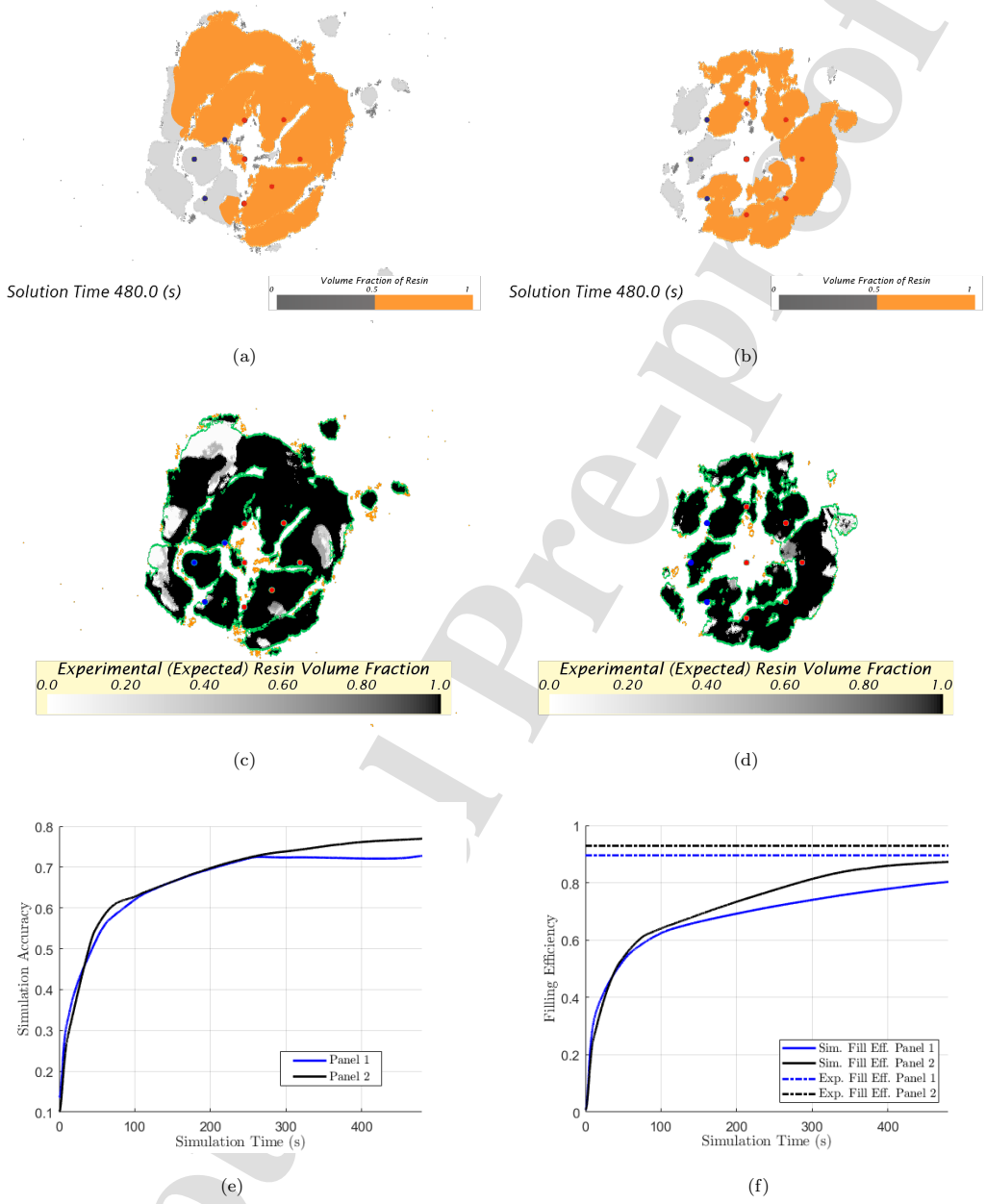

Figure 10: Validation results: Final state of the injection simulation of (a) Panel 1 and (b) Panel 2 (in all simulations, orange indicates resin and grey indicates air); experimental volume fraction of resin of (c) Panel 1 and (d) Panel 2; (e) simulation accuracy index throughout the simulation, based on comparing the simulation and experiment results; and (f) fill efficiency over the course of both simulations compared to the expected fill efficiency based on experiments.

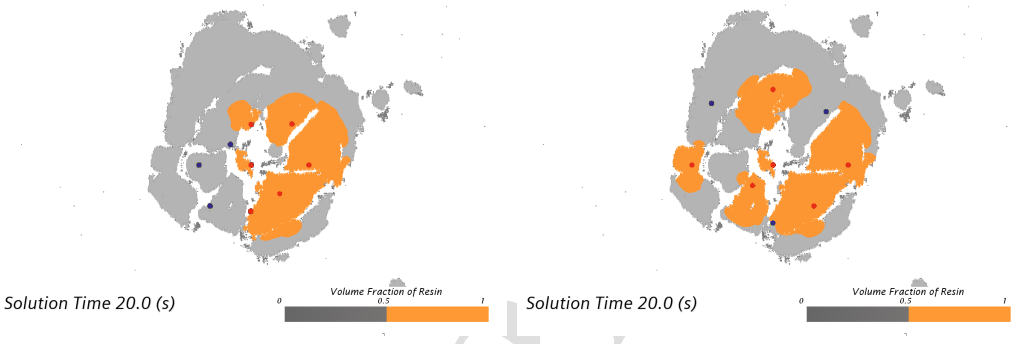

(a) (b)

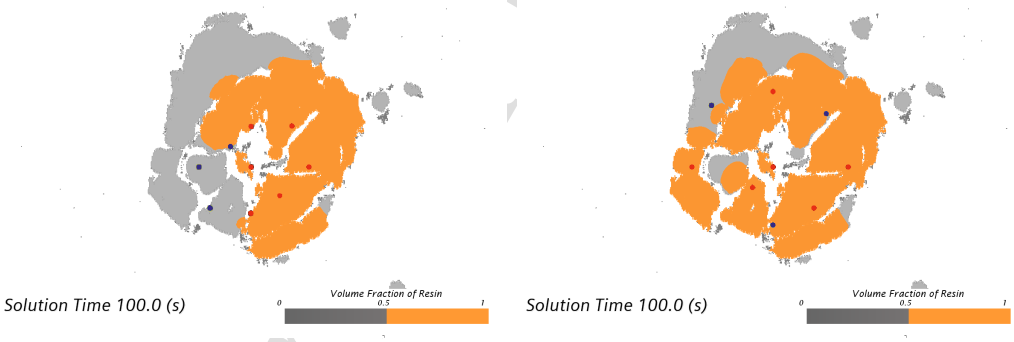

(c) (d)

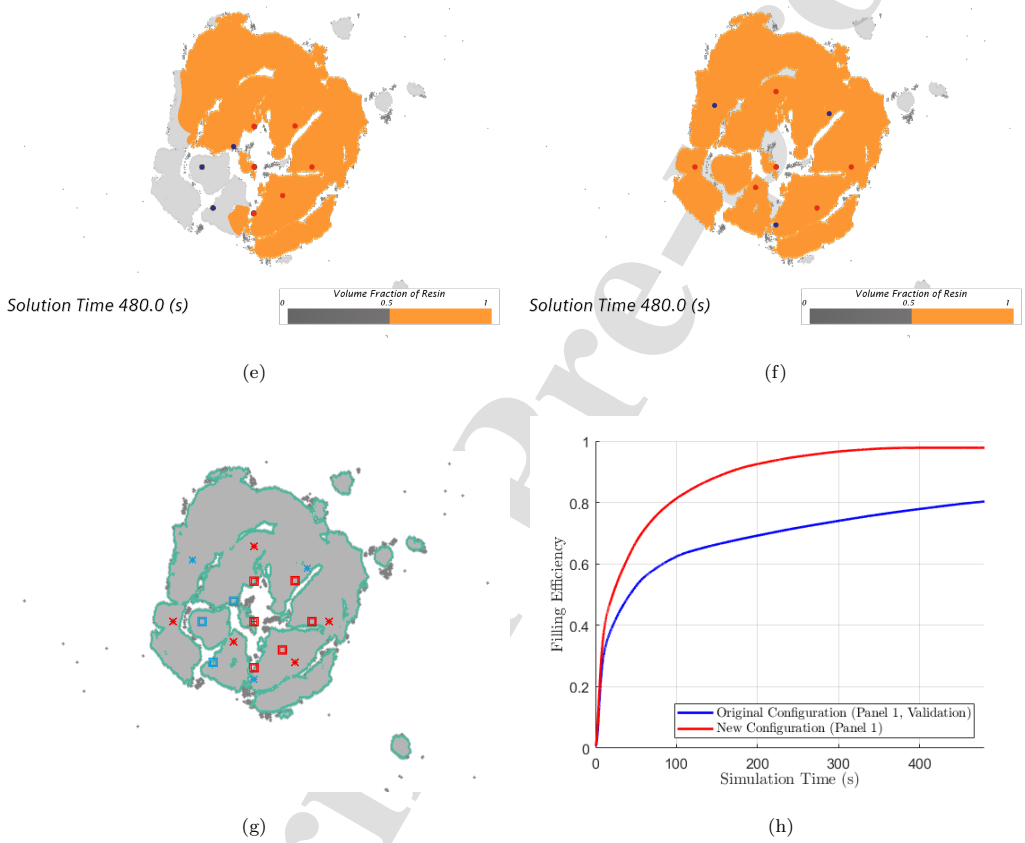

(e) (f)

(g) (h)

Figure 11: Study case: Simulation progression of Panel 1 with the (a), (c), (e) original configuration used in validation; and with the (b), (d), (f) new configuration. Configurations shown overlaid in (g) with square indicating the validation configuration, while 'x' shows the new configuration. Fill efficiency of the two simulations illustrated in (h).

Highlights:

- A proof-of-concept for the simulation of resin injection repair
- Geometry of the damage area and the simulation parameters are obtained via c-scans
- An analytical solution of two-phase porous flow case is proposed for verification
- Method is validated on impacted panels and shows 70+% simulation accuracy
- Method identifies suitable injection configurations whilst allowing in situ repair

Ahmed Asiliskender: Methodology; Software; Validation; Formal analysis; Investigation; Data Curation; Writing - Original Draft; Writing - Review & Editing; Visualization

Joaquim Peiró: Conceptualization; Writing - Review & Editing; Supervision; Project administration; Funding acquisition

Koon-Yang Lee: Conceptualization; Writing - Review & Editing; Supervision; Funding acquisition

Apostolos Parlamas: Investigation; Resources

Brian Falzon: Resources; Writing - Review & Editing

Zafer Kazancı: Resources; Writing - Review & Editing

Declaration of interests

☐ The authors declare that they have no known competing financial interests or personal relationships that could have appeared to influence the work reported in this paper.

☒ The authors declare the following financial interests/personal relationships which may be considered as potential competing interests:

Joaquim Peiro reports financial support was provided by Defence Science and Technology Laboratory.